nature electronics

ARTICLES

https://doi.org/10.1038/s41928-022-00732-y

Check for updates

Gigahertz topological valley Hall effect in nanoelectromechanical phononic crystals

Qicheng Zhang[1,5], Daehun Lee[2,5], Lu Zheng[2], Xuejian Ma[2], Shawn I. Meyer[2], Li He[1], Han Ye[3], Ze Gong[4], Bo Zhen[1], Keji Lai[2]✉ and A. T. Charlie Johnson[1,4]✉

Topological phononic crystals can manipulate elastic waves that propagate in solids without being backscattered, and could be used to develop integrated acousto-electronic systems for classical and quantum information processing. However, acoustic topological metamaterials have been mainly limited to macroscale systems that operate at low (kilohertz to megahertz) frequencies. Here we report a topological valley Hall effect in nanoelectromechanical aluminium nitride membranes at gigahertz (up to 1.06 GHz) frequencies. We visualize the propagation of elastic waves through phononic crystals with high sensitivity (10–100 fm) and spatial resolution (10–100 nm) using transmission-mode microwave impedance microscopy. The valley Hall edge states, which are protected by band topology, are observed in both real and momentum space. Robust valley-polarized transport is evident from wave transmission across local disorder and around sharp corners. We also show that the system can be used to create an acoustic beamsplitter.

Topological phases of matter have non-trivial boundary states that are protected by the global property of bulk energy bands and are thus robust against local perturbations[1–3]. Topological band theory was originally developed for electron waves in condensed-matter systems, but soon expanded into other wave systems, leading to advances in topological mechanics[4,5], photonics[6,7] and phononics[8,9]. Transport through edge channels in topological phononic systems is particularly protected from backscattering due to structural disorders, fabrication imperfections and environmental changes[10–20]. The development of artificial elastic structures with novel band topology (metamaterials) could thus be of technological value, particularly when the configurations created are suitable for integrated circuit applications.

Topological phases of matter have been established via coordinated efforts in theoretical calculations, experimental implementation and systematic characterization. In electronic materials, this is achieved by using first-principles calculations, material synthesis, macroscopic transport, momentum-space (k-space) mapping and microscopic imaging[2]. The same design principles also apply to acoustic metamaterials[8,9,21], whose elastic moduli or mass densities vary periodically on a scale comparable to the acoustic wavelength. To date, studies of topological phononic crystals have been limited to relatively low frequencies. In the kilohertz range, the sonic design can be implemented by a periodic arrangement of centimetre-scale metamolecules (such as rods, rings or prisms), and the local pressure field of the sound wave can be measured with a microphone[13–15,18]. In the megahertz range, the local displacement field of the elastic wave can be detected by a scanning laser interferometer[16,17,19,20].

Topological phononic crystals that operate in the ultrahigh frequency (UHF; 0.3–3.0 GHz) and super-high-frequency (SHF; 3.0–30.0 GHz) bands—which are important in wireless communication[22], sensing[23] and universal quantum interconnects[24]—are less explored. This is due, in part, to the difficulties involved in probing phononic structures fabricated on monolithic substrates. In particular, optical vibrometers[16,17,19,20] with diffraction-limited spatial resolution (around 1 μm) are not generally applicable in the UHF/SHF (0.3–30.0 GHz) regime due to the micrometre-scale gigahertz acoustic wavelength in solids.

In this Article, we report the development of gigahertz topological valley Hall insulators based on microfabricated free-standing aluminium nitride (AlN) membranes and the observation of robust valley-polarized edge states in phononic crystals. Using transmission-mode microwave impedance microscopy (TMIM)[25,26], we observe the wave pattern across gapped and gapless phononic crystals. Edge transport channels are seen at the interface between two domains with opposite valley Chern numbers, and band dispersion is consistent with reciprocal-space analysis using fast Fourier transform (FFT). The edge transport is robust against local disorder at the domain wall, as well as sharp corners in Z-shaped channels. We also demonstrate topology-protected wave steering, creating an acoustic analogue to an optical beamsplitter.

Phononic crystal design

Our topological nanoelectromechanical structure is based on the phononic analogue of the valley Hall effect (VHE)[27]. Valley pseudospin[28] labels the degenerate energy extrema in momentum space, whose topological nature stems from the non-trivial Berry curvature localized at these extremal points of the acoustic band structure. As depicted in Fig. 1a, snowflake-like[29,30] regions are etched away from a free-standing AlN membrane[31,32]. The rhombic primitive cell consists of two sublattice sites (equilateral triangles, radii of circumcircles $r_0 \pm \delta r$) and linking bridges. Figure 1b shows the calculated band structures using finite-element modelling (Methods). The dependence of eigenfrequencies as a function of various dimensions of this snowflake pattern is shown in Supplementary Section 1. When $\delta r = 0$, the structure can be viewed as an acoustic analogue of graphene, with C_{6v} symmetry (sixfold rotations about the snowflake centre and mirror symmetry about the vertical planes

[1]Department of Physics and Astronomy, University of Pennsylvania, Philadelphia, PA, USA. [2]Department of Physics, University of Texas at Austin, Austin, TX, USA. [3]State Key Laboratory of Information Photonics and Optical Communications, Beijing University of Posts and Telecommunications, Beijing, China. [4]Department of Materials Science and Engineering, University of Pennsylvania, Philadelphia, PA, USA. [5]These authors contributed equally: Qicheng Zhang, Daehun Lee. ✉e-mail: kejilai@physics.utexas.edu; cjohnson@physics.upenn.edu

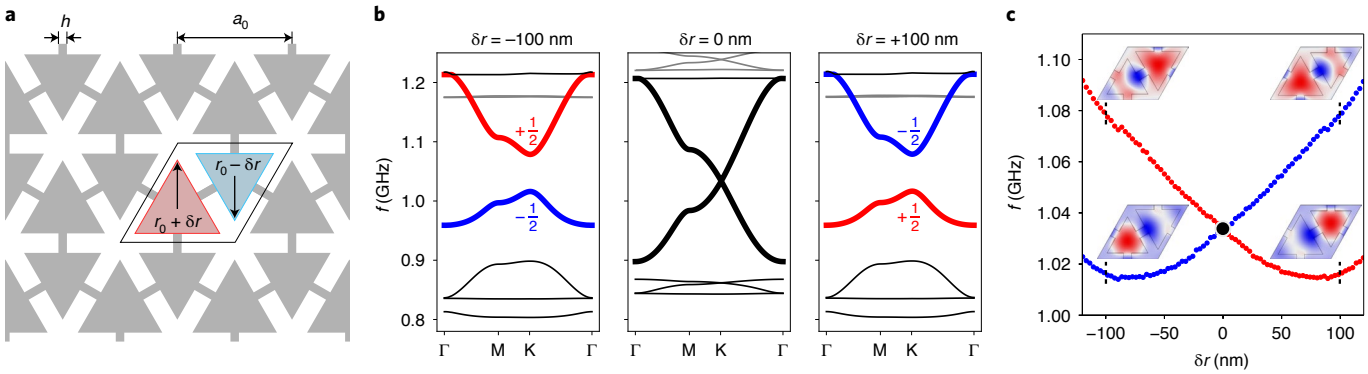

Fig. 1 | Phononic crystal design and calculated band structures. a, Schematic of the metamaterial design. The white regions are etched away from a free-standing AlN membrane. The rhombus indicates the unit cell, which consists of two equilateral triangles and connecting bridges. Parameters in the figure are $a_0 = 4.90\,\mu m$, $r_0 = 2.00\,\mu m$, $h = 0.36\,\mu m$ and $\delta r = +100\,nm$. Only δr is varied among the different samples. **b**, Left to right: simulated band structures with $\delta r = -100$, 0 and 100 nm. The topological bands relevant to this work are highlighted. Dirac dispersion is observed in the middle structure ($\delta r = 0$). The valley Chern numbers near the band extrema are labelled for the gapped structures. **c**, Eigenfrequencies at the top/bottom band edges of interest as a function of δr. The black dot denotes the band-closing point and valley Hall phase transition at $\delta r = 0$. The insets depict the eigenmodes of piezoelectric potential within a unit cell at the band extrema for $\delta r = \pm 100$ nm.

containing a basis vector of the honeycomb lattice), resulting in time-reversal-symmetry-protected Dirac dispersion near the K and K′ points of the Brillouin zone. For $\delta r \neq 0$, the symmetry of the phononic crystal reduces to C_{3v} and the broken inversion symmetry lifts the degeneracy at the Dirac point[14,15,18,20,33–35]. Figure 1c shows the δr-dependent bandgaps and piezoelectricity-induced electrical potential profiles at the band edges for $\delta r = \pm 100$ nm. The topological phase transition across $\delta r = 0$ can be captured by an effective $\mathbf{k}\cdot\mathbf{p}$ Hamiltonian[14]:

$$H_{K(K')} = v_D\left(\kappa_x\sigma_x + \kappa_y\sigma_y + mv_D\sigma_z\right), \quad (1)$$

where v_D is the Dirac velocity, $\kappa_{x,y,z}$ is the momentum deviation from the K (K′) point, $\sigma_{x,y,z}$ is the Pauli matrix and m is the mass term introduced by the broken inversion symmetry. This massive Dirac Hamiltonian produces non-trivial Berry curvatures at the two valleys, each of which can be integrated into a topological charge, that is, a valley Chern number $C_{K(K')} = 1/2(\mathrm{sgn}(m))$ (ref. [14]). Here $\mathrm{sgn}(m)$ refers to the sign of m. It should be noted that because of the large momentum separation between the inequivalent K and K′ valleys, intervalley scattering is often substantially suppressed. As shown below, the quantization of $C_{K(K')}$, arising from mass inversion and the assumption of inhibited intervalley scattering, plays crucial roles in the emergence of gapless valley Hall edge states.

The design of our phononic crystal is geometric in nature and fully compatible with standard nanofabrication processes[31,32]. Figure 2a, inset, shows the nanoelectromechanical device fabricated on a free-standing 800-nm-thick c-axis polycrystalline AlN film. Future experiments could incorporate Sc-doped AlN thin films[36] that will further improve the electromechanical coupling. We emphasize that compared with an earlier work[16], the relatively thick and stiff film and the small dimensions of the triangular artificial atoms are crucial for the realization of gigahertz characteristic frequencies. The phononic crystal is patterned by electron-beam lithography and plasma etching. The interdigital transducers (IDTs) used to excite acoustic waves in the film are formed by depositing 45-nm-thick Al on piezoelectric AlN.

Characterization of gapless and gapped phononic crystals

The visualization of gigahertz acoustic waves is performed by TMIM on an atomic force microscopy (AFM) platform[25,26]. All the measurements are performed under ambient temperature and pressure. As illustrated in Fig. 2a, the acoustic wave is launched by the emitter IDT. The shielded cantilever probe[37] behaves as a microwave receiver to pick up the ~1 GHz piezoelectric potential. Through the 50 Ω impedance-match section, the signal is amplified and demodulated by an in-phase/quadrature (I/Q) mixer, using the same microwave source that drives the emitter IDT. The signals at the radio-frequency (RF) and local oscillator (LO) ports of the mixer can be expressed as $V_{RF} \propto e^{i(\omega t - kx)}$ and $V_{LO} \propto e^{i(\omega t + \theta)}$, where ω is the angular frequency, k is the acoustic wavevector and θ is the mixer phase. The two output channels are, therefore, $V_{Ch1} \propto \mathrm{Re}\left(V_{RF}V_{LO}^*\right) = \cos\left(kx + \theta\right)$ and $V_{Ch2} \propto \mathrm{Im}\left(V_{RF}V_{LO}^*\right) = -\sin\left(kx + \theta\right)$. The complex-valued TMIM signal $V_{Ch1} + iV_{Ch2}$ provides a phase-sensitive measurement on the local displacement field of the elastic wave. For simplicity, we will only present one channel below, unless otherwise specified. The unique properties of the TMIM setup include (1) high sensitivity (~10–100 fm)[38], superior to that of commercial laser-based scanning vibrometers (~1 pm)[39]; (2) high spatial resolution (~10–100 nm), well into the nanoscale; and (3) high operation frequency up to 10 GHz and beyond[26], making it an ideal technique to study integrated UHF/SHF phononic metamaterials.

We begin by characterizing the gap opening due to broken space-inversion symmetry. As illustrated in Fig. 2a, the phononic crystal region is tilted from the normal of the plane wave launched by the IDT. The conservation of momentum parallel to the phononic crystal boundary[14] requires that $k_{\parallel} = k_0 \sin\phi$, where $k_{\parallel}$ is the projection of K (or K′) on the boundary, k_0 is the wavevector for the pattern-free AlN membrane and ϕ is the tilt angle. As shown in Supplementary Section 2, this angular selection rule is satisfied at $\phi_1 = 23°$ (Figs. 3–5) and $\phi_2 = 55°$ (Fig. 2). In Fig. 2b,c, we plot the transmission spectra (obtained using a vector network analyser) of the gapless and gapped structures, respectively. Within the IDT passband (1.00–1.06 GHz), the transmission coefficient (S_{21}) of the gapless phononic crystal is substantially higher (~30 dB) than that of the gapped phononic crystal. The residual wave transmission in the gapped phononic crystal is consistent with tunnelling across the finite-sized (50 μm) crystal via an evanescent mode. The corresponding TMIM images at 1.045 GHz are shown in Fig. 2d,e. For the design with $\delta r = 0$, the gapless nature is evident from the appearance of transmitted plane waves on the opposite side of the phononic crystal. In contrast, for the gapped structure ($\delta r = 100$ nm), the phononic crystal region in the TMIM image (Fig. 2e) only displays snowflake patterns due to topographic crosstalk

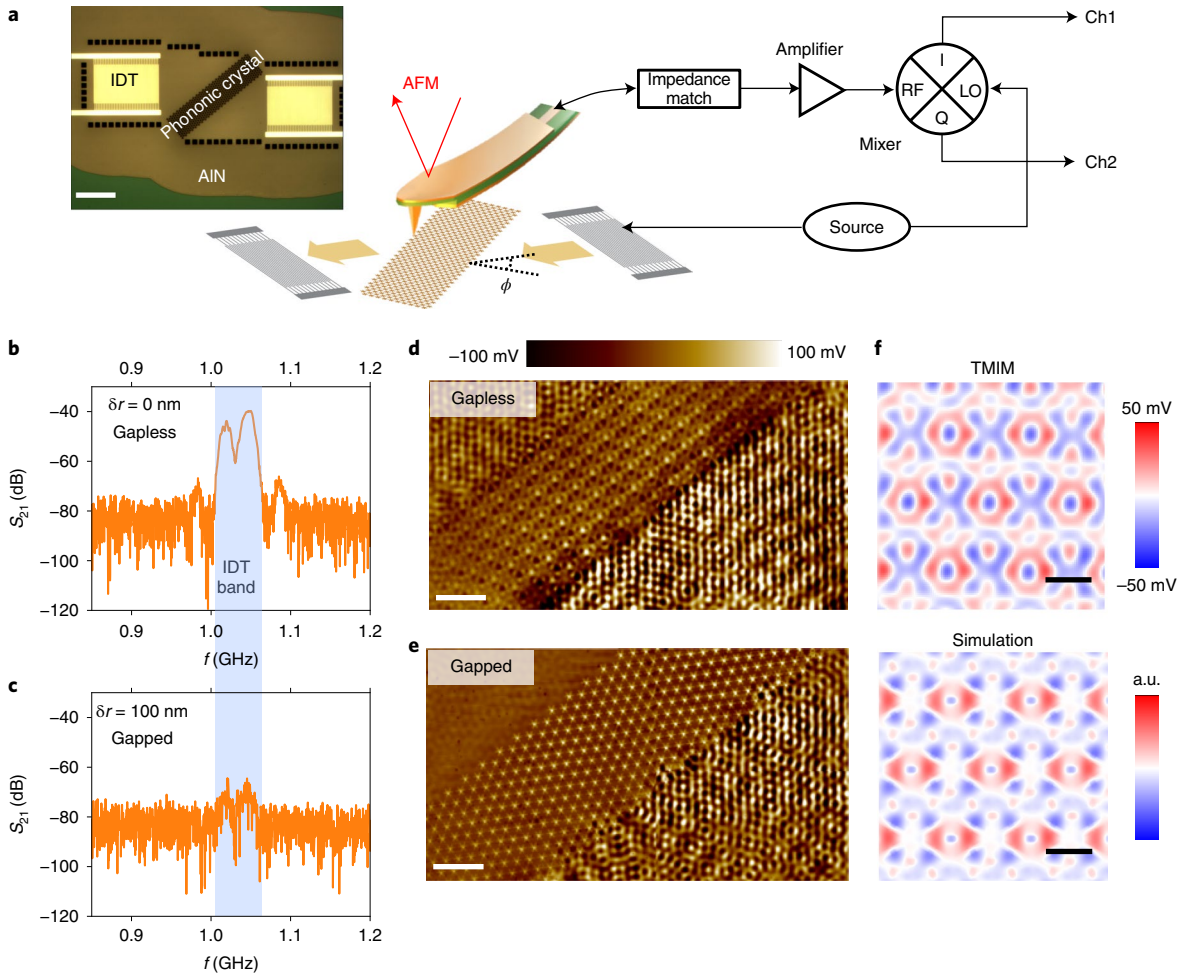

Fig. 2 | Characterization of gapless and gapped phononic crystals. a, Left, picture of a phononic device fabricated on a suspended AlN membrane. Right, schematic of the TMIM setup and acoustic device with input/output IDTs (shown in grey). Ch1 and Ch2 are two output channels with a phase difference of $\pi/2$. **b**,**c**, Transmission coefficient (S_{21}) as a function of excitation frequency for the gapless device with $\delta r = 0$ nm (**b**) and gapped device with $\delta r = 100$ nm (**c**). The IDT passband is shaded in blue in both plots. **d**,**e**, TMIM images at $f = 1.045$ GHz corresponding to **b** (**d**) and **c** (**e**). **f**, TMIM image inside the gapless phononic crystal in **d**, plotted in a different false-colour map. The lower image shows the simulated piezoelectric potential profile for the same field of view. Scale bars, 40 μm (**a**), 20 μm (**d** and **e**) and 5 μm (**f**).

(Supplementary Section 3), and the transmitted wave on the far side of the phononic crystal is much weaker than for the gapless system (Fig. 2d). In addition, Fig. 2f shows the TMIM image inside the gapless phononic crystal and the potential profile simulated by finite-element modelling. The resemblance between the two images confirms that the TMIM indeed measures the piezoelectric surface potential, which is proportional to the acoustic displacement field on the AlN membrane.

Valley Hall edge states

Figure 3a displays a scanning electron microscopy image around the interface separating the two domains with $\delta r = +100$ nm (top) and $\delta r = -100$ nm (bottom). Since the difference in topological charge between the two domains is quantized, that is, $|\Delta C_K| = 1$, a chiral valley Hall edge mode must exist at the boundary due to the bulk–edge correspondence[14]. Figure 3b shows the real-space TMIM image at the upper bound of the IDT passband ($f = 1.060$ GHz), where a weak channel carrying elastic waves is observed (Supplementary Section 4 provides the complete data). The k-space information can be obtained by taking the FFT of the signal $V_{Ch1} + iV_{Ch2}$. Using the extended Brillouin zone of the honeycomb lattice (Fig. 3c) as a guide, we can discern a faint high-intensity line on the left side of the K point (Fig. 3d). At $f = 1.045$ GHz (Fig. 3e), which coincides with the frequency at the K point in reciprocal space, the valley Hall edge state is fully resolved as the frequency is well within the IDT band. Correspondingly, the FFT map (Fig. 3f) exhibits very strong intensity at the K point. According to Bloch's theorem[40], the wavefunction of the edge state satisfies $\psi_{\vec{k}}(\vec{r}) = u_{\vec{k}}(\vec{r})e^{i\vec{k}\cdot\vec{r}}$, where $u_{\vec{k}}(\vec{r})$ is a function with lattice periodicity. At the K point, where $|k_x| = 2\pi/3a_0$, one should expect a period of $3a_0$ in the wavefunction, that is, $\psi_K(x + 3a_0) = \psi_K(x)$, as indeed observed in Fig. 3e. We emphasize that the weak intensity at the K′ valley (Fig. 3f) is not due to intervalley scattering. Rather, it is associated with the inevitable reflection due to the impedance mismatch at the junction between the phononic crystal region and the unpatterned region, which leads to wave propagation in the opposite direction (Supplementary Section 5). At $f = 1.010$ GHz, the frequency lies inside the bulk band such that both bulk and edge states are present (Fig. 3g). The k-space map (Fig. 3h) also shows a high-intensity line on the right side of the K point, which is associated with the valley Hall edge state, as well as some intensity around the K point, which indicates the appearance of bulk states.

The high-resolution FFT maps allow us to quantitatively compare the experimental data and the calculated band structure. In

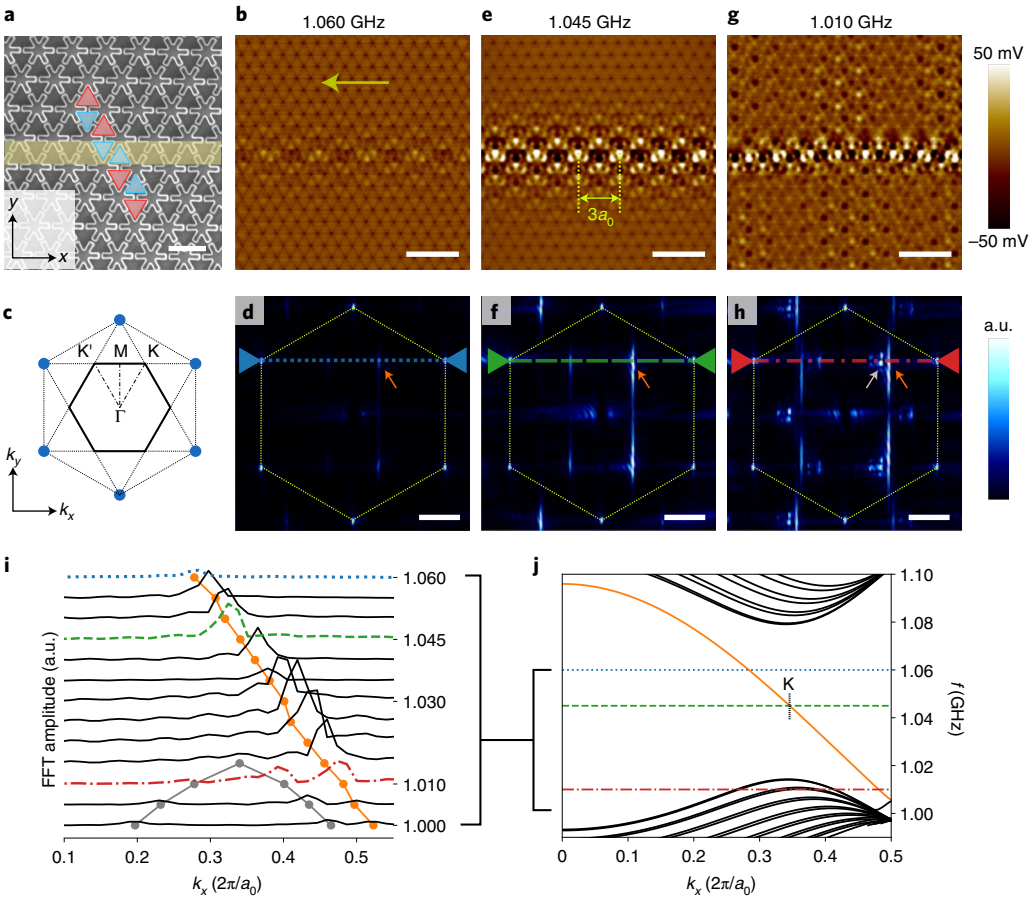

Fig. 3 | Real-space imaging and momentum-space analysis of valley Hall edge states. a, Scanning electron microscopy image near the interface (shaded in yellow) between two valley Hall insulators with $\delta r = +100$ nm (top) and $\delta r = -100$ nm (bottom). The two sublattice sites are marked as blue and red triangles for clarity. **b**, TMIM image of the topological valley Hall edge state taken at $f = 1.060$ GHz. The arrow indicates that the elastic wave is launched from the right IDT and propagates in the $-x$ direction. **c**, Generic k-space map of the honeycomb lattice. The solid hexagon is the first Brillouin zone, with the high-symmetry points labelled in the map. The blue dots represent the reciprocal lattice sites. **d**, FFT amplitude map for the TMIM data at $f = 1.060$ GHz. The dashed hexagon is a guide for comparison with **c**. The high-intensity line (orange arrow) is associated with the valley Hall edge state. **e**,**f**, TMIM image (**e**) and FFT map (**f**) at $f = 1.045$ GHz. The wave pattern of the VHE exhibits a period of $3a_0$. **g**,**h**, TMIM image (**g**) and FFT map (**h**) at $f = 1.010$ GHz. The bulk states are visible in both real-space and k-space (denoted by the grey arrow) data. **i**, Measured FFT amplitude along K–K′ from 1.00 to 1.06 GHz. The blue, green and red curves are extracted from the profiles indicated by the horizontal lines (between the two triangles) of the corresponding colours in **d**, **f** and **h**. The peak positions of the edge and bulk states are marked by orange and grey dots, respectively. **j**, Simulated bands of the phononic crystal projected in the k_x direction, showing the valley Hall edge band running across the bulk gap. The horizontal lines indicate the three representative frequencies of the corresponding colours in **i**. The valley Hall edge state is coloured in orange. Scale bars, 5 μm (**a**), 20 μm (**b**, **e** and **g**) and $2\pi \times 0.05\,\mu m^{-1}$ (**d**, **f** and **h**).

real space, the valley Hall edge state is a gapless mode localized at the interface and travels along opposite directions near K and K′ valleys because of the opposite group velocity, manifesting the momentum-valley locking of the chiral edge states. The group velocity is characterized by band dispersion as $d\omega/dk$. In Fig. 3i, we display the FFT line profiles along the K–K′ direction and highlight the three representative frequencies shown in Fig. 3b–h. The dispersion of both bulk and topological edge states is clearly seen as we track the position of the FFT peak intensity. This is in excellent agreement with the simulated curves in Fig. 3j, where the simulated bands projected in the k_x direction are plotted. Here a single band appears around the K valley and runs monotonically across the bulk bandgap of 1.015–1.080 GHz.

Using the same topological design, we can also demonstrate the robustness of valley Hall edge state transport against structural imperfections. Figure 4a illustrates the schematic of a different phononic crystal sample with one defect (three missing snowflakes) at the domain boundary[13]. As shown in Fig. 4b, although the signal strengths in both channels are altered by the scatterer, the TMIM modulus ($\sqrt{V_{Ch1}^2 + V_{Ch2}^2}$) remains unchanged after crossing the local disorder. In other words, the scattering centre modifies the phase but not the amplitude of the elastic wave propagating along the topological interface. Similarly, the topological protection of valley transport is also validated by transmission with negligible loss through sharp corners of a zigzag interface[14] (Fig. 4c, inset). At the unit-cell level, the relative position of the two valley Hall domains is invariant with respect to the interface. As a result, the forward-moving modes are always projected onto the same valley and protected from backscattering by the band topology. As shown in the TMIM image (Fig. 4c), the incident elastic wave is guided into the domain wall and freely propagates through the two sharp turns. The absence of wave attenuation across the corners is evident from the TMIM signal profiles at three representative locations (Fig. 4c, bottom-right inset). The exponential decay ($e^{-x/\xi}$) of the wavefunction into gapped phononic crystal regions indicates that the valley

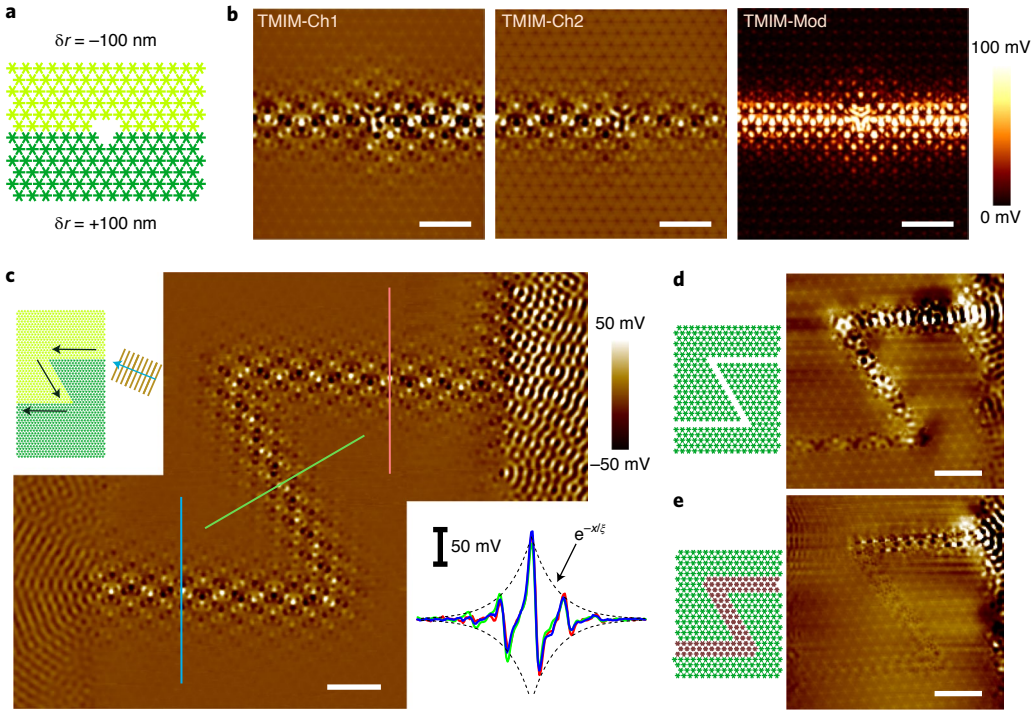

Fig. 4 | Robustness of valley Hall edge transport. a, Schematic of a local defect (three missing snowflakes) at the valley Hall interface. **b**, Left to right: TMIM-Ch1, TMIM-Ch2 and TMIM-modulus images of the sample in **a**. The disorder alters the phase but not the amplitude of the elastic wave travelling along the topological boundary. **c**, TMIM image of a Z-shaped valley Hall edge channel (schematic, top-left inset). The bottom-right inset shows the line profiles at three representative locations denoted in the image. The dashed lines are exponential fits ($e^{-x/\xi}$, where ξ is the characteristic length) to the envelope function of the TMIM amplitude. **d**,**e**, TMIM images of a Z-shaped pattern-free channel (**d**) and a Z-shaped gapless channel embedded in gapped crystals (**e**). The schematic is shown to the left of the corresponding image. Substantial reflection and attenuation are evident for these topologically trivial interfaces. The false-colour scale for all the TMIM images is from −50 to 50 mV. Scale bars, 20 μm.

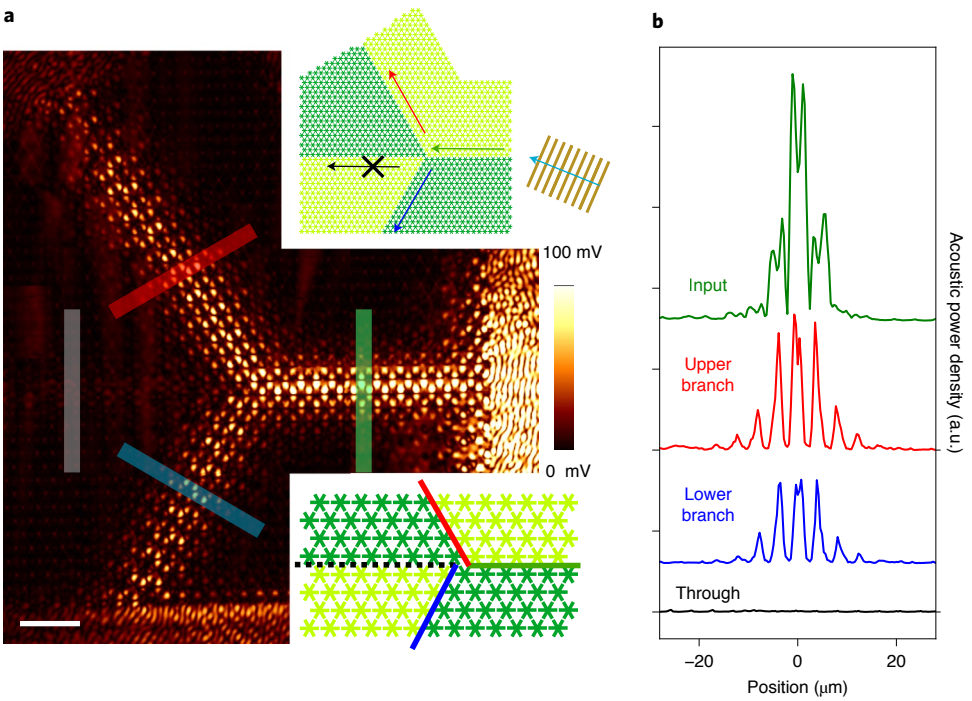

Fig. 5 | Demonstration of topological beamsplitting. a, TMIM-modulus image of a topological beamsplitter based on four alternating domains (schematic, top-right inset). The bottom-right inset shows a close-up view around the intersection. Scale bar, 20 μm. **b**, Square of TMIM-modulus signals integrated over one wavelength, which is proportional to the acoustic power, for the four paths labelled in **a**.

Hall edge state is indeed localized at the topological interface, where $\xi \approx 6\,\mu m$ comparable to the lattice constant. For comparison, we design and measure two topologically trivial Z-shaped channels—one pattern-free waveguide (Fig. 4d) and one gapless waveguide (Fig. 4e)—within gapped phononic crystals. In both cases, the first 120° turn already introduces substantial reflection and strong disturbance to the incident wave. The attenuation after two bending corners is so strong that little energy is transmitted to the output port. The topological protection is, therefore, crucial for guiding elastic waves with minimal loss in nanoelectromechanical systems.

Topological beamsplitter

Finally, we demonstrate a VHE-based topological beamsplitter[33,41]. Figure 5a shows the TMIM-modulus image as an elastic wave enters a metastructure with four alternating valley Hall domains (schematic, top-right inset). The incident wave splits into two branches separated by an angle of 120°. On the other hand, the appearance of a propagating wave along the straight route after splitting would indicate that the wave is scattered to the other valley at the junction, which is prohibited by VHE. In the experiment, wave transmission in the forward direction beyond the intersection is indeed negligible, with a suppression factor of over 40 dB. Interestingly, a careful examination of the crystal design (Fig. 5a, bottom-right inset) indicates that the upper branch is closer to the input line than the lower branch by $0.5a_0$. This subtle asymmetry is readily captured by the sensitive TMIM imaging. In Fig. 5b, we plot the square of TMIM-modulus image integrated over one wavelength ($\int_{a_0} \left(V_{\mathrm{Ch1}}^2 + V_{\mathrm{Ch2}}^2\right) \mathrm{d}x$), which is proportional to the acoustic power, for all the four segments. The lower branch receives less (~40%) acoustic energy than the upper branch (~60%) from the incident wave, which is consistent with the uneven beamsplitting inherent in the metamaterial design.

The gigahertz topological VHE demonstrated in this work may be exploited for integrated phononic circuits in the UHF/SHF regime. An acoustic beamsplitter (for example, Fig. 5a) can be used as power dividers or combiners. The zigzag valley Hall edge channels (Fig. 4c) allow robust one-dimensional transport with a small footprint, which is suitable for compact acoustic delay lines. Moreover, the valley-momentum locking property will enable us to implement valley filters. Here the gapless state ($\delta r = 0$) is used as the background phononic crystal, where the valley degree of freedom is well defined. In this 'acoustic graphene', both K and K′ valley-polarized states can propagate in all the directions allowed by crystal symmetry. One can then construct a topological VHE region (similar to Fig. 3a) to select a specific valley state. After certain circuit operations, the valley information can be read out by passing it through a second VHE region that has either the same or opposite valley polarity. All these circuit elements are promising candidates for classical and quantum information applications.

Conclusions

We have reported gigahertz nanoelectromechanical phononic crystals with topologically non-trivial structures. Using microwave impedance microscopy, we visualized the elastic wave on patterned piezoelectric AlN membranes. The topologically protected edge states between two gapped structures with opposite valley Chern numbers were observed via both real-space imaging and momentum-space analysis. The valley Hall edge state protected against backscattering is evident from the negligible loss through local disorders and sharp corners, as well as power splitting into multiple edge channels. Our work provides a framework to develop integrated topological phononics for use in classical and quantum information processing in the microwave regime.

Methods

Device fabrication. We fabricated phononic structures on 800-nm-thick *c*-axis polycrystalline AlN films grown by magnetron sputtering on Si wafers. The phononic crystal was formed by electron-beam lithography and plasma etching of AlN using 660-nm-thick SiN_x hard mask. IDTs were used to emit and receive phonons. The IDT fingers have an aperture width of 80 μm. The IDTs were fabricated by electron-beam lithography and lift-off of 45-nm-thick aluminium. Finally, the AlN film was released from the Si substrate by a XeF_2 etcher.

Finite-element modelling. The band structures and potential profiles are calculated using finite-element methods using COMSOL Multiphysics 5.4 software. We compute the one- and two-dimensional band structures along with the potential profiles in the corresponding geometries with periodic boundary conditions. Here 'piezoelectric effect multiphysics' is applied, which couples the solid mechanics module and electrostatics module. The material properties used are slightly modified from the reported AlN membrane properties[42]. Specifically, $c_{11} = c_{22} = 375\,\mathrm{GPa}$, $c_{12} = 125\,\mathrm{GPa}$, $c_{13} = c_{23} = 120\,\mathrm{GPa}$, $c_{33} = 435\,\mathrm{GPa}$, $c_{44} = c_{55} = 118\,\mathrm{GPa}$, $c_{66} = (c_{11} - c_{12})/2 = 125\,\mathrm{GPa}$, $e_{31} = e_{32} = -0.58\,\mathrm{C\,m^{-2}}$, $e_{33} = 1.55\,\mathrm{C\,m^{-2}}$, $e_{15} = e_{24} = -0.48\,\mathrm{C\,m^{-2}}$ and $\rho = 3{,}180\,\mathrm{kg\,m^{-3}}$[43].

Experimental set. TMIM is implemented on an AFM platform (Park AFM, XE-70). The shielded cantilever probe (model 5-300N) is commercially available from PrimeNano. At ~1 GHz, the cantilever probe can be viewed as a lumped element with an effective capacitance of ~1 pF. An impedance-match network is needed to route the tip to the 50 Ω transmission lines, resulting in a measurement bandwidth of ~70 MHz. In the experiment, this band is tuned to match the passband of the IDT. The tip/impedance-match receiver has an effective input impedance $|Z_{\mathrm{in}}|$ of ~1 kΩ at 1 GHz. Through a similar tip–sample coupling impedance Z'_{t_s} of ~100 kΩ, an input signal is picked up by the tip and then amplified and demodulated by the microwave electronics. The details of the TMIM experiment can be found elsewhere[25]. All the measurements are performed at room temperature.

Data availability

The raw data that support the findings of this study are available from the corresponding authors upon reasonable request.

Received: 4 September 2021; Accepted: 18 February 2022;
Published online: 28 March 2022

References

1. Fu, L., Kane, C. L. & Mele, E. J. Topological insulators in three dimensions. *Phys. Rev. Lett.* **98**, 106803 (2007).
2. Hasan, M. Z. & Kane, C. L. Topological insulators. *Rev. Mod. Phys.* **82**, 3045 (2010).
3. Qi, X.-L. & Zhang, S.-C. Topological insulators and superconductors. *Rev. Mod. Phys.* **83**, 1057 (2011).
4. Süsstrunk, R. & Huber, S. D. Observation of phononic helical edge states in a mechanical topological insulator. *Science* **349**, 47–50 (2015).
5. Nash, L. M. et al. Topological mechanics of gyroscopic metamaterials. *Proc. Natl Acad. Sci. USA* **112**, 14495–14500 (2015).
6. Lu, L., Joannopoulos, J. D. & Soljačić, M. Topological photonics. *Nat. Photon.* **8**, 821–829 (2014).
7. Ozawa, T. et al. Topological photonics. *Rev. Mod. Phys.* **91**, 015006 (2019).
8. Ma, G., Xiao, M. & Chan, C. T. Topological phases in acoustic and mechanical systems. *Nat. Rev. Phys.* **1**, 281–294 (2019).
9. Liu, Y., Chen, X. & Xu, Y. Topological phononics: from fundamental models to real materials. *Adv. Funct. Mater.* **30**, 1904784 (2020).
10. Khanikaev, A. B., Fleury, R., Mousavi, S. H. & Alu, A. Topologically robust sound propagation in an angular-momentum-biased graphene-like resonator lattice. *Nat. Commun.* **6**, 8260 (2015).
11. Mousavi, S. H., Khanikaev, A. B. & Wang, Z. Topologically protected elastic waves in phononic metamaterials. *Nat. Commun.* **6**, 8682 (2015).
12. Yang, Z. et al. Topological acoustics. *Phys. Rev. Lett.* **114**, 114301 (2015).
13. He, C. et al. Acoustic topological insulator and robust one-way sound transport. *Nat. Phys.* **12**, 1124–1129 (2016).
14. Lu, J. et al. Observation of topological valley transport of sound in sonic crystals. *Nat. Phys.* **13**, 369–374 (2017).
15. Zhang, Z., Tian, Y., Cheng, Liu, X. & Christensen, J. Experimental verification of acoustic pseudospin multipoles in a symmetry-broken snowflakelike topological insulator. *Phys. Rev. B* **96**, 241306(R) (2017).
16. Cha, J., Kim, K. W. & Daraio, C. Experimental realization of on-chip topological nanoelectromechanical metamaterials. *Nature* **564**, 229–233 (2018).
17. Yan, M. et al. On-chip valley topological materials for elastic wave manipulation. *Nat. Mater.* **17**, 993–998 (2018).
18. Han, X. et al. Experimental demonstration of acoustic valley Hall topological insulators with the robust selection of C_{3v}-symmetric scatterers. *Phys. Rev. Appl.* **12**, 014046 (2019).
19. Yan, M. et al. Pseudomagnetic fields enabled manipulation of on-chip elastic waves. *Phys. Rev. Lett.* **127**, 136401 (2021).
20. Ma, J., Xi, X. & Sun, X. Experimental demonstration of dual-band nano-electromechanical valley-Hall topological metamaterials. *Adv. Mater.* **33**, 2006521 (2021).

21. Cummer, S. A., Christensen, J. & Alu, A. Controlling sound with acoustic metamaterials. *Nat. Rev. Mater.* **1**, 16001 (2016).
22. Hashimoto, K.-Y. *Surface Acoustic Wave Devices in Telecommunications: Modelling and Simulation* (Springer, 2000).
23. Ballantine Jr, D. et al. *Acoustic Wave Sensors: Theory, Design and Physico-Chemical Applications* (Elsevier, 1996).
24. Chu, Y. et al. Quantum acoustics with superconducting qubits. *Science* **358**, 199–202 (2017).
25. Zheng, L., Wu, D., Wu, X. & Lai, K. Visualization of surface-acoustic-wave potential by transmission-mode microwave impedance microscopy. *Phys. Rev. Appl.* **9**, 061002 (2018).
26. Zheng, L., Shao, L., Loncar, M. & Lai, K. Imaging acoustic waves by microwave microscopy. *IEEE Microw. Mag.* **21**, 60–71 (2020).
27. Mak, K. F., McGill, K. L., Park, J. & McEuen, P. L. The valley Hall effect in MoS_2 transistors. *Science* **344**, 1489–1492 (2014).
28. Xu, X., Yao, W., Xiao, D. & Heinz, T. F. Spin and pseudospins in layered transition metal dichalcogenides. *Nat. Phys.* **10**, 343–350 (2014).
29. Brendel, C., Peano, V., Painter, O. J. & Marquardt, F. Pseudomagnetic fields for sound at the nanoscale. *Proc. Natl Acad. Sci. USA* **114**, E3390–E3395 (2017).
30. Brendel, C., Peano, V., Painter, O. J. & Marquardt, F. Snowflake phononic topological insulator at the nanoscale. *Phys. Rev. B* **97**, 020102(R) (2018).
31. Gorisse, M. et al. Observation of band gaps in the gigahertz range and deaf bands in a hypersonic aluminum nitride phononic crystal slab. *Appl. Phys. Lett.* **98**, 234103 (2011).
32. Ghasemi Baboly, M., Alaie, S., Reinke, C. M., El-Kady, I. & Leseman, Z. C. Ultra-high frequency, high *Q*/volume micromechanical resonators in a planar AlN phononic crystal. *J. Appl. Phys.* **120**, 034502 (2016).
33. Ye, L. et al. Observation of acoustic valley vortex states and valley-chirality locked beam splitting. *Phys. Rev. B* **95**, 174106 (2017).
34. Vila, J., Pal, R. K. & Ruzzene, M. Observation of topological valley modes in an elastic hexagonal lattice. *Phys. Rev. B* **96**, 134307 (2017).
35. Wang, M., Ye, L., Christensen, J. & Liu, Z. Valley physics in non-Hermitian artificial acoustic boron nitride. *Phys. Rev. Lett.* **120**, 246601 (2018).
36. Colombo, L. et al. Investigation of 20% scandium-doped aluminum nitride films for MEMS laterally vibrating resonators. In *2017 IEEE International Ultrasonics Symposium (IUS)* 1–4 (IEEE, 2017).
37. Yang, Y. et al. Batch-fabricated cantilever probes with electrical shielding for nanoscale dielectric and conductivity imaging. *J. Micromech. Microeng.* **22**, 115040 (2012).
38. Lee, D. et al. Direct visualization of gigahertz acoustic wave propagation in suspended phononic circuits. *Phys. Rev. Appl.* **16**, 034047 (2021).
39. *PICOSCALE Vibrometer System Controller PV-CTRL-V1.0*. https://www.smaract.com/controllers-accessories/product/picoscale-vibrometer?download=files/media/categories/Optical%20Metrology/Spec-Sheets/PV-SS_CTRL-V1.0_SpecSheet.pdf (SmarAct, 2021).
40. *Ultra High Frequency and Full-Field Vibration Analysis Performance Testing of Microsystems*: *Application Note*. https://www.polytec.com/fileadmin/website/vibrometry/pdf/OM_AN_VIB_U_003_UHF_Scanning_E_42426.pdf (Polytec, 2016).
41. Kittel, C. *Introduction to Solid State Physics* (John Wiley & Sons, 2005).
42. Wang, Z. et al. Multichannel topological transport in an acoustic valley Hall insulator. *Phys. Rev. Appl.* **15**, 024019 (2021).
43. Gerfers, F. et al. Sputtered AlN thin films for piezoelectric MEMS devices—FBAR resonators and accelerometers. in *Solid State Circuits Technologies* (ed Swart, J. W.) Ch. 17 (IntechOpen, 2010).

Acknowledgements

A.T.C.J., Q.Z. and Z.G. acknowledge support by the NSF through the Laboratory for Research on the Structure of Matter, an NSF Materials Research Science & Engineering Center (MRSEC; DMR-1720530). K.L., D.L., L.Z., X.M. and S.I.M. acknowledge support by the NSF's Division of Materials Research award DMR-2004536 and Welch Foundation grant F-1814 for the TMIM work. Data analysis was partially supported by the NSF through the Center for Dynamics and Control of Materials, an NSF MRSEC under Cooperative Agreement DMR-1720595. This work was carried out in part at the Singh Center for Nanotechnology, which is supported by the NSF National Nanotechnology Coordinated Infrastructure Program under grant NNCI-2025608. B.Z. and L.H. acknowledge support for the metamaterial design and simulation work by the US Office of Naval Research (ONR) Multidisciplinary University Research Initiative (MURI) grant N00014-20-1-2325 on Robust Photonic Materials with High-Order Topological Protection and grant N00014-21-1-2703. H.Y. acknowledges support of the National Natural Science Foundation of China (grant no. 11974003). We would like to express our appreciation for useful discussions with T. Olsson and Q. Niu.

Author contributions

A.T.C.J. and K.L. conceived the project. Q.Z. fabricated the phononic devices and performed the band-structure simulations. D.L. and L.Z. performed the TMIM imaging and data analysis. X.M. and S.I.M. contributed to the TMIM data analysis. L.H., Z.G., H.Y. and B.Z. contributed to the phononic crystal design. Q.Z., D.L. and K.L. drafted the manuscript with contributions from all the authors. All the authors have given approval to the final version of the manuscript.

Competing interests

The authors declare no competing interests.

Additional information

Supplementary information The online version contains supplementary material available at https://doi.org/10.1038/s41928-022-00732-y.

Correspondence and requests for materials should be addressed to Keji Lai or A. T. Charlie Johnson.

Peer review information *Nature Electronics* thanks Yan-Feng Chen, Zhengyou Liu and the other, anonymous, reviewer(s) for their contribution to the peer review of this work.